Topological Persistence of Heterogeneous Sandstone

Anna L Herring[1], Vanessa Robins[1], Mohammad Saadatfar[1], BenjaminYoung[2], Mark Knackstedt[1], Adrian Sheppard[1]

[1]Department of Applied Mathematics, Research School of Physics & Engineering, The Australian National University, Canberra, ACT, Australia
[2]Thermo Fisher Scientific, Brno, Czech Republic

This paper was prepared for presentation at the International Symposium of the Society of Core Analysts held in Trondheim, Norway, 27-30 August 2018

ABSTRACT

Quantitative topological analysis of the internal pore space architecture of porous rocks, and of the fluid distributions within the pore space, has recently been utilized to inform understanding and predictions of petrophysical properties such as permeability, fluid relative permeability, and nonwetting phase capillary trapping capacity and efficiency. So far, this type of analysis has only been utilized effectively for relatively homogenous media, partially due to the intrinsic nature of topology: topological analysis inherently disregards geometry and size of features; it provides quantification of the connectivity and interconnectivity of a phase (i.e. pore space or fluid), but no information on the relevant length scales of connections or isolated components. This presents problems for analysis of heterogeneous media, where fluid flows are strongly influenced by the relative size and spatial variation of preferential pathways.

Persistent homology is a technique which complements standard topological analysis because it measures the size of topological features (disconnected components and redundant connections) as well as the frequency of each kind of feature. This capability to link topology and geometry results in a powerful analytical tool; for example, this type of analysis has recently been used to develop a universal capillary trapping relationship that describes nonwetting phase trapping during capillary-dominated imbibition flows for a variety of homogenous sandstones.

Here, persistent homology analysis is applied (via the open-source image analysis program Diamorse) to a drainage-imbibition experiment in a heterogeneous reservoir sandstone exhibiting, notably, a high density cement layer in the lower quarter of the core and a lateral fracture above the layer. Steady-state drainage and imbibition processes were carried out in a vertical fluid injection (flow from bottom to top), and 3D internal phase distributions were measured after each flow process using pore-scale helical trajectory X-ray computed tomography (CT) via the CTLab at the Australian National University (ANU). Nonwetting phase (octane) saturation levels after drainage and after imbibition were measured for subsections of the core as well as for the entirety of the core, and are shown to relate to persistent homology signatures measured for the pore space and the initial octane distribution.

INTRODUCTION

There is a growing body of research linking the topology of the pore space and fluid phases within a porous medium to physical flow properties relevant to engineering applications. Recently, topology has been identified as a significant predictor of conductivity [1], absolute permeability [2], [3], fluid relative permeability [4], and nonwetting phase capillary trapping efficiency [5], [6]; it has been suggested that topology provides a potential metric to describe the complete thermodynamic state of a multiphase fluid-porous medium system [7], and a descriptor for fluid flow front morphologies during unsteady-state drainage processes [8], as well as during steady state injections which may be dominated by "connected pathway" vs. "ganglion dynamics" flows [9]. These studies utilize the Euler characteristic (χ) of a fluid phase, generally measured using 3D image analysis of X-ray tomography experiments, to quantify fluid phase topology:

$$\chi = \beta_0 - \beta_1 + \beta_2 \quad (1)$$

In Eq. 1, β_0 is the number of individual components (individual ganglia) of a phase, β_1 is the number of redundant internal connections within a phase (for a fluid phase, this counts the number of redundant pore throats occupied by the fluid), and β_2 is the number of cavities, or holes within the phase (for nonwetting fluids, β_2 is unphysical and is neglected). For a more complete description of fluid phase χ as a function of fluid saturation, we refer to [5], [6].

As exemplified by Eq. 1, topology (as quantified by β_0, β_1, β_2, and χ) inherently provides a measurement of the connectivity and interconnectivity of a phase, but not the size or shape of any connected or disconnected components comprising that phase. This dictates that topological metrics are particularly sensitive to noise and other small features in 3D images, indicating that noisy images, or images which are acquired under different conditions or processed using different regimes may produce dramatically different values of χ or β numbers when measured using image analysis.

Persistent homology is an image analysis technique which complements standard topological analysis because it measures the sizes of all β_0, β_1, and β_2 features; the frequency of each kind of feature; and the "persistence" of each feature- essentially, the size range over which a particular topological feature exists [10]–[12]. Persistent homology has previously been used to inform understanding of crystallization [13] and critical length scales for percolation [10] of dry granular systems. For application to multiphase fluid flow, [14] used persistent homology to measure the size, frequency, and persistence of pore bodies and redundant pore throats filled with nonwetting phase fluid; this information was used to develop a "persistent homology based aspect ratio" which was shown to correlate with nonwetting phase capillary trapping for three different (homogenous) sandstones under a wide range of initial saturation conditions and image acquisition parameters. This study aims to investigate whether this analysis can accurately describe fluid flow in heterogeneous samples as well.

EXPERIMENTAL METHODS

The drainage-imbibition experiment was conducted in an ANU-developed high pressure flow cell (Figure 1), specifically designed for implementation with ANU laboratory-based helicalX-ray CT data acquisition [15]. The system is comprised of four pumps: two hydraulic oil pumps (Metarock Laboratories, Houston, TX, United States) control radial confining and axial fluid pressure, and two Hastelloy pumps (Teledyne ISCO, Lincoln, NE, United States) control injection fluids. Stainless steel tubing (1/16th inch OD) and Swagelok connections (Swagelok, Solon OH, United States) connect the pumps, pressure monitoring dials, and safety pressure release valves; flexible PEEK tubing was used to connect to the flow cell, allowing for smooth rotation and vertical translation of the core holder during scanning. Fluids (brine and octane in these experiments) were pumped into the bottom of the core via two separate inlets (Figure 1a); all fluid exits the top of the core via one flow line, which in connected in-line to a zero-flow back pressure regulator with electronic pilot control (Equilibar Precision Pressure Control, Fletcher, North Carolina, United States). Pump control and data collection is facilitated by Metarock©-developed software.

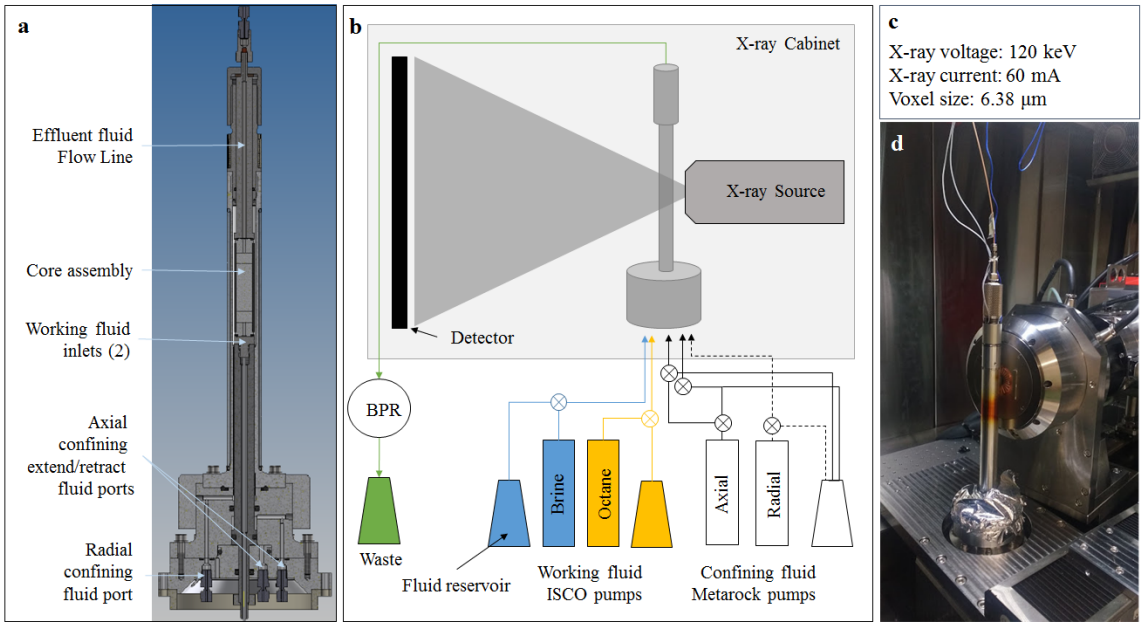

Figure 1. Experimental system used for the drainage-imbibition flow experiment. The sandstone core was installed in the ANU-manufactured core holder (a); which is installed in the X-ray CT cabinet and connected via PEEK flow lines to confining and working fluid pumps, and the back pressure regulator (BPR), as shown in the schematic (b). Image acquisition parameters are reported (c), and a photograph of the core holder as installed in front of the X-ray source is shown (d).

The reservoir sandstone sample ("DC10t") is a fine to medium well sorted laminated sandstone sourced from the Otway basin in Victoria. The sample was cored to 12 mm diameter and cut to approx. 38 mm length; the core plug was bounded on both ends by viton o-rings, sintered copper flow diffusers, and endcaps; and incased in shrinkwrap,

which acts a barrier between the confining pressure fluid and the experimental fluids. The core was installed inside an aluminum 7075 (T6511 temper) core holder (manufactured in-house at the ANU), and axial pressure was applied by tightening the upper endcap until vertical displacement (of approx. 0.001 mm) of the core was measured via an internal linear variable differential transformer. At this point, axial pressure was applied via pumping confining fluid (hydraulic oil, Multitherm IG-4) into the axial fluid chamber of the core holder to a pressure of approx. 100 PSI, after which confining fluid was pumped into the radial region between the shrinkwrap and the core holder walls and elevated to 50 PSI. Axial and radial confining pressure were then elevated simultaneously to a working pressures of 350 and 300 PSI, respectively.

The "dry" scan was acquired after axial and confining pressure was applied, prior to any fluid injection. After dry scan acquisition, the core was saturated with 0.5 M KI brine at relatively high flow rate (i.e. the fastest flow rate that maintained brine pore pressure < 300 PSI, as reported by the internal pressure transducer). Then, the pore pressure was incrementally increased to 250 PSI by increasing the back pressure regulator pressure setting, while still flowing brine, to attempt to simultaneously dissolve any remaining air bubbles and flush them from the core. Some air bubbles were still present after this process; however, the region used for image analysis in this study (Figure 2) exhibited 98.1% brine saturation. Pore pressure was maintained via constant pressure operation of the brine pump while a scan was acquired in this saturated state. Drainage was carried out by injecting octane at 1.8 ml/min for a total of 10 estimated pore volumes; after which pore pressure was maintained at 250 PSI via the octane pump for the duration of the initial state scan. Finally, brine was imbibed at a constant flow rate of 0.18 ml/min (corresponding to a Darcy velocity of $2.65 \cdot 10^{-5}$ m/s) for 20 pore volumes to reach nonwetting phase residual saturation; and pore pressure was maintained at 250 PSI via the brine pump while the residual scan was acquired. Radiographs were acquired during each flow process to monitor the extent of flow and to check that a steady state was achieved before acquisition of the tomogram (i.e. no changes were observed over dozens of consecutive radiographs spanning decades of minutes). Data acquisition parameters for the experimental run are reported in Figure 1c. All scans required approx. 20 hours and were collected as Region of Interest (ROI) scans using a double helix acquisition pattern.

ANALYTICAL METHODS

Grayscale tomograms (Figure 2a) were segmented into two phases (pore space vs grain phase for the dry scan, and nonwetting phase vs. combined wetting/grain phase for partially saturated states) using a converging active contours (CAC) algorithm [16]; and segmentations were denoised of small speckle noise (isolated speckles <64 voxels) in both phases (Figure 2b). The original volume (5.75 mm x 5.75 mm x 37.0 mm) was divided into six subsections to investigate sub-sample heterogeneity (Figure 2d); analysis was also carried out on the total volume as well.

Persistent homology signatures were measured using the open-source program Diamorse. The complete process is detailed elsewhere [10,11], and only briefly described here. First,

a signed Euclidean distance transform (SEDT) is calculated from the segmented data (Figure 2c; Figure 3b); this transform calculates the distance for every voxel in the image to the nearest phase 0-1 boundary. The sign in the SEDT distinguishes distances for the two phases; for this application, negative values indicate distances measured from within the pore/nonwetting phase while positive values indicate distances measured from the solid/combined solid-wetting phase. A level set filtration of the SEDT is performed (Figure 3c-d), starting at the largest negative values (center of the largest pore/nonwetting bodies) and progressing to the largest positive values (center of the largest grains/grain conglomerates): at each distance value topological features are identified. The appearance of a β feature is termed its "birth", the merging of a β_0 with another, or the closing in of β_1 or β_2 feature is termed its "death", and the difference between the two values is termed the "persistence" of a feature. Over the course of the level set filtration, the distance values for birth and death, dimension (i.e. 0, 1, or 2), and location of each birth and death event is recorded, and can be plotted in what is known as a persistent homology "signature". Through this process, topological features of the sandstone pore space and the nonwetting phase are identified, and linked to their size and persistence.

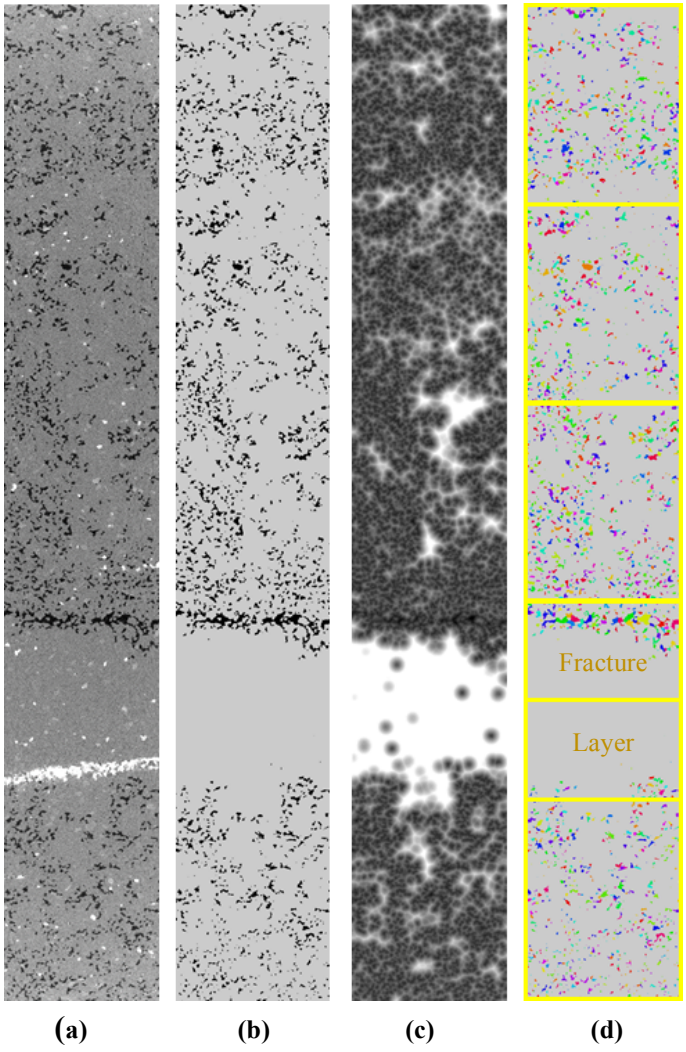

Figure 2. Image processing sequence for the initial (post-drainage) state of reservoir sandstone DC10t. Grayscale X-ray tomograms (a) were segmented into two phases (b): nonwetting phase (octane, black), and combined solid/wetting phase (gray). A signed Euclidean distance transform (SEDT; c; distance values indicated in bottom right legend) was calculated from the 3D segmentation; and persistent homology signatures are calculated on level-set filtrations of the SEDT. The 3D data (total volume: 5.75 mm x 5.75 mm x 37.0 mm) were cropped into six smaller subvolumes for analysis as indicated by the boxes in (d), which also shows color-labeled individual β_0 features of the nonwetting phase as measured during the persistent homology analysis. Subvolumes containing significant features ("fracture" and "layer") are labeled here and in subsequent figures.

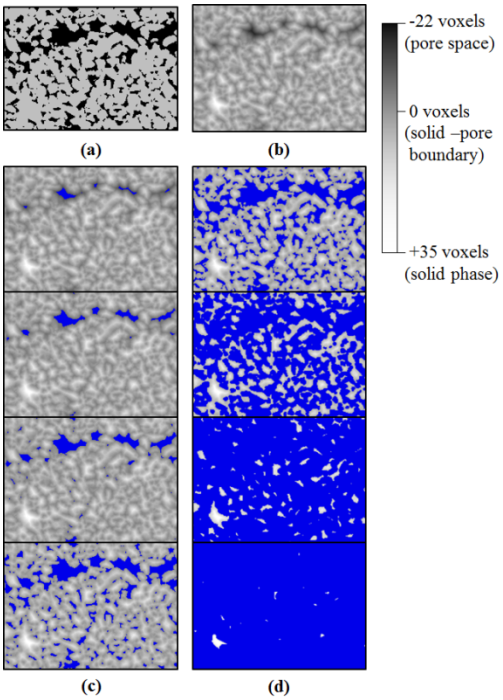

Figure 3. Persistent homology filtration of a subset of the dry sandstone sample. From the segmented data (a), a signed Euclidean distance transform (SEDT) is calculated (b); the grayscale shown in the SEDT corresponds to distances from the pore-grain boundary as indicated by the legend on the right. Topological values (β_0, β_1, β_2) are calculated for the active phase (indicated in blue in (c) and (d)) for each iteration of the level-set filtration of the SEDT. The filtration starts at the largest negative values (in the pore space) and the level-set value increases to the largest positive values (in the solid phase). Progressive filtrations through the pore space are shown from top-to-bottom in (c); the filtration reaches the zero distance value (i.e. active blue phase is equivalent to the segmented pore space in (a)) in the top frame of (d), and increases into the grain phase from top-to-bottom in (d).

In the following section, values derived from the persistent homology signatures are shown to correlate with fluid saturations after flow processes. The values we identify are defined in Equations 2-4.

$$PH_{\beta_1} = \sum_i [b_i \times (d_i - b_i)] \quad (2)$$

$$PH_{\beta_0} = \sum_j [b_j \times (d_j - b_j)] \quad (3)$$

In these equations, b is the level-set distance value of each feature birth, indicating the feature's size, and the quantity $(d\text{-}b)$ is the topological persistence of each feature; subscript i indicates the index for all β_1 features with $b<0$ and $d>0$ (i.e. redundant connections, or throats), and subscript j indicates the index for all β_0 features (equivalent to pore/ganglia bodies). Thus, the metrics defined in equations 2-3 provide a combined quantification of the number, size, and persistence of redundant connections/pore throats (PH_{β_1}) and ganglia/pore bodies (PH_{β_0}).

In order to examine the effect of these topologic features on capillary trapping levels during imbibition, a composite metric, the "persistent homology based aspect ratio" is used [14]:

$$PH_{\frac{\beta_1}{\beta_0}} = \frac{PH_{\beta_1}}{PH_{\beta_0}} \times (voxel\ resolution)^3 \quad (4)$$

In Eq. 4, image voxel resolution cubed is incorporated to indicate size (capillary trapping is a small-length scale phenomenon, only relevant at length scales at which capillarity applies); this factor also allows for comparison of the value measured from the current data with the results from other imaging studies.

The $PH_{\frac{\beta_1}{\beta_0}}$ formulation can be considered similarly to traditional indices of pore networks such as aspect ratio (ratio of pore throat size to pore body size) and coordination number (number of pore throats connected to a single pore body); but in this analysis "bodies" (i.e. β_0 features) and "throats" (β_1 features) are defined from a topological perspective. A large PH_{β_1} value indicates there are numerous, large, and/or spatially persistent redundant connections (throats, or nonwetting phase connections through throats); in contrast, a large PH_{β_0} value indicates there are numerous, large, and/or spatially isolated pore/ganglia bodies. Thus, large $PH_{\frac{\beta_1}{\beta_0}}$ values indicate fluid configurations favoring nonwetting fluid mobilization, while small values indicate configurations more favorable to nonwetting phase trapping.

RESULTS

Persistent homology signatures were measured for subvolumes and the total data volume (as indicated in Figure 2) for two data sets: the pore space of the dry sample (imaged prior to any fluid injection) and the octane phase of the "initial" sample stage (imaged after the completion of the steady-state drainage; i.e. 10 PV octane injection). Initial octane volumes ($V_{I,\ NW}$) are correlated with β_1 values (Eq. 2) measured from the persistent homology signatures of the dry samples (Figure 4a). Trapped octane volume efficiency (residual octane volume normalised by initial octane volume, $V_{R,NW}/V_{I,\ NW}$) is correlated with the aspect ratio $PH_{\beta1/\beta0}$ (Eq. 4) measured from the octane phase present at the initial state (Figure 4b). The physical interpretation of these results supports conventional understanding of drainage and imbibition processes, as described below.

During drainage, nonwetting phase invasion is impeded by small pore throats, while relatively large pore throats are more easily invaded [e.g., 16]. Data subsections with high values of $PH_{\beta1}$ contain redundant pathways which are more numerous, larger, and/or more persistent; thus, these regions are favorable to nonwetting fluid invasion, resulting in higher volume displaced during drainage. This relationship is shown to apply to the core subsections, which exhibit a range of $PH_{\beta1}$ values (Figure 4a); the $PH_{\beta1}$ value and volume displaced for the full core volume is also shown for context.

During imbibition, the amount of nonwetting fluid which becomes trapped is partially dictated by the topology of that fluid at its initial state: a fluid phase which is comprised of numerous, large, and/or more persistent redundant connections (relative to the ganglia body centers identified as β_0 features) is likely to be mobilized, and exhibits a correspondingly large $PH_{\beta1/\beta0}$ value. On the other hand, if redundant connections are fewer, smaller, and less spatially persistent relative to the larger ganglia body centers, the measured $PH_{\beta1/\beta0}$ value will be smaller and capillary trapping efficiency (quantified as volume of residual nonwetting phase normalized by initial nonwetting phase in each respective volume: $V_{R,NW}/V_{I,NW}$) will be larger. This relationship is illustrated in Figure 4b, where the relationship measured for sample DC10t is compared to the previously measured relationship comprising three relatively homogenous sandstones (Bentheimer, Berea, and Leopard; detailed results reported in [14]). Both data sets exhibit a negative

semi-log relationship between capillary trapping efficiency and $PH_{\beta1/\beta0}$, although the slope of each trendline is different. This difference in slope is likely due to differences in fluid properties (octane in the DC10t experiment vs. air in the homogenous sandstone experiments) and flow conditions (Darcy velocity of $2.65 \cdot 10^{-5}$ m/s in the DC10t experiment vs. $3.29 \cdot 10^{-7}$ m/s for the homogenous sandstones). Again, the full core value is included in Figure 4b for additional context; the trendline is calculated from subvolume data.

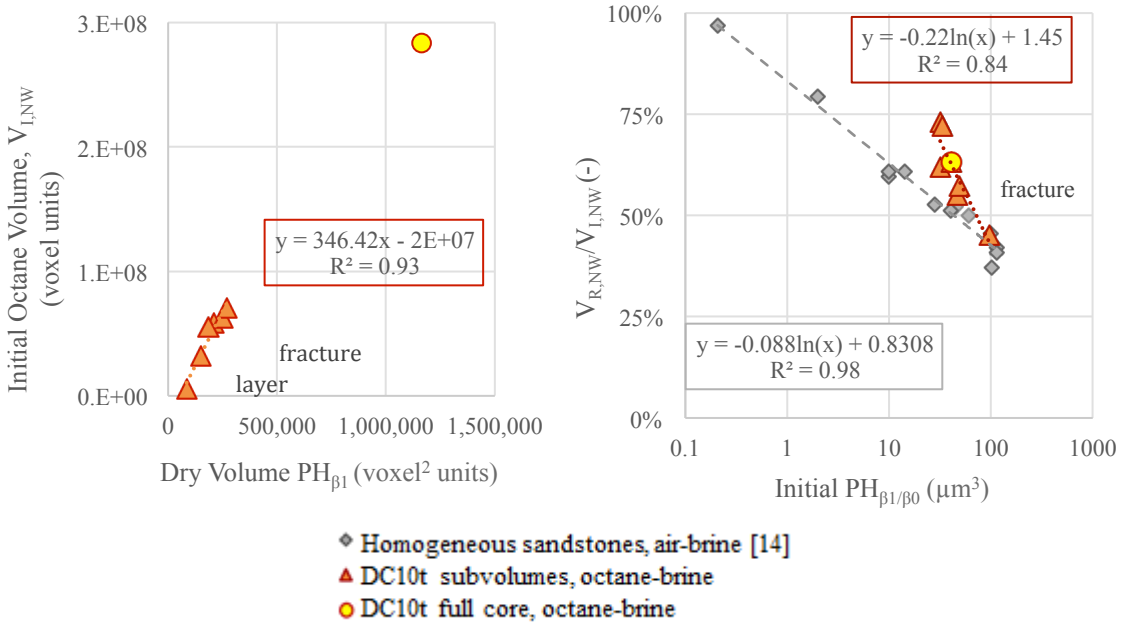

Figure 4. Experimental results. (a) The $PH_{\beta1}$ values measured for the dry sample subvolumes and total volume are correlated with the initial octane volume, $V_{I,\ NW}$, present at the end of drainage. (b) The persistent homology based aspect ratio, $PH_{\beta1/\beta0}$, measured from the initial nonwetting phase distribution, is correlated with the fraction of nonwetting phase which is capillary trapped ($V_{R,\ NW}/V_{I,\ NW}$) after the subsequent imbibition process. Trendlines and R^2 values are calculated from subvolume data points.

CONCLUSIONS

Persistent homology image analysis provides a means to measure both the topology and geometry of a phase. Here, we investigate 3D X-ray tomographic images of a cement-layered and fractured heterogeneous sandstone, at dry and initial (post-drainage) saturation conditions, using persistent homology (via the program Diamorse). We measure the summed size and persistence of internally redundant connections, $PH_{\beta1}$; and the summed size and spatial persistence of distinct bodies, $PH_{\beta0}$. From these values we also calculate the composite "persistent homology based aspect ratio", $PH_{\beta1/\beta0}$. We find that measured topological signatures of the sample at each state are correlated to the fluid invasion and mobilization during subsequent flow processes. Specifically:

(1) $PH_{\beta1}$ of the pore space dictates the nonwetting phase occupancy ($V_{I,NW}$) after nonwetting phase injection (drainage).

(2) $PH_{\beta1/\beta0}$ of the octane phase in the drained sample dictates the subsequent nonwetting phase trapping efficiency ($V_{R,NW}/V_{I,NW}$) after imbibition.

The presence of strong correlations between the persistent homology measured values $PH_{\beta 1}$ and $PH_{\beta 1/\beta 0}$, and nonwetting phase occupancy after drainage and after imbibition, provides evidence of the applicability and strength of this analytical tool to investigate how regional (subvolume) and global (total volume) topology and geometry will impact fluid flow processes; even for layered, fractured, and heterogeneous samples such as the DC10t sample investigated here.

ACKNOWLEDGEMENTS

We gratefully acknowledge financial assistance provided through CO2CRC and Australian National Low Emissions Coal Research and Development (ANLEC R&D). ANLEC R&D is supported by Australian Coal Association Low Emissions Technology Limited and the Australian Government through the Clean Energy Initiative. We also acknowledge funding through the member companies of the ANU/UNSW Digicore Research Consortium, as well as the Australian Research Council: Adrian Sheppard is supported by Discovery Project DP160104995, Vanessa Robins is supported by ARC Future Fellowship FT140100604, and Anna Herring is supported by ARC Discovery Early Career Fellowship DE180100082. We also wish to thank Tim Sawkins and Ron Cruikshank for contributing to experimental component design and manufacture.

REFERENCES

[1] K. Mecke and C. H. Arns, "Fluids in porous media: a morphometric approach," *J. Phys. Condens. Matter*, vol. 17, pp. 503–534, 2005.
[2] C. Scholz, F. Wirner, J. Götz, U. Rüde, G. E. Schröder-Turk, K. Mecke, and C. Bechinger, "Permeability of Porous Materials Determined from the Euler Characteristic," *Phys. Rev. Lett.*, vol. 109, no. 26, p. 264504, Dec. 2012.
[3] Z. Liu, A. L. Herring, V. Robins, and R. T. Armstrong, "Prediction of Permeability from Euler Characteristic of 3D Images," in *International Symposium of the Society of Core Analysts*, 2017.
[4] Z. Liu, A. Herring, C. Arns, S. Berg, and R. T. Armstrong, "Pore-Scale Characterization of Two-Phase Flow Using Integral Geometry," *Transp. Porous Media*, pp. 1–19, Mar. 2017.
[5] A. L. Herring, L. Andersson, S. Schlüter, A. Sheppard, and D. Wildenschild, "Efficiently Engineering Pore-Scale Processes: Force Balance and Topology During Nonwetting Phase Trapping in Porous Media," *Adv. Water Resour.*, vol. 79, pp. 91–102, 2015.
[6] A. L. Herring, E. J. Harper, L. Andersson, A. Sheppard, B. K. Bay, and D. Wildenschild, "Effect of fluid topology on residual nonwetting phase trapping: Implications for geologic CO2 sequestration," *Adv. Water Resour.*, vol. 62, pp. 47–58, Dec. 2013.
[7] J. E. McClure, M. A. Berrill, W. G. Gray, and C. T. Miller, "Influence of phase connectivity on the relationship among capillary pressure, fluid saturation, and interfacial area in two-fluid-phase porous medium systems," *Phys. Rev. E*, vol. 94, no. 3, p. 33102, Sep. 2016.
[8] S. Schlüter, S. Berg, M. Rücker, R. T. Armstrong, H.-J. Vogel, R. Hilfer, and D. Wildenschild, "Pore-scale displacement mechanisms as a source of hysteresis for two-phase flow in porous media," *Water Resour. Res.*, vol. 52, no. 3, p. n/a-n/a, Mar. 2016.
[9] M. Rücker, S. Berg, R. T. Armstrong, A. Georgiadis, H. Ott, A. Schwing, R. Neiteler, N. Brussee, A. Makurat, L. Leu, M. Wolf, F. Khan, F. Enzmann, and M. Kersten, "From connected pathway flow to ganglion dynamics," *Geophys. Res. Lett.*, May 2015.
[10] V. Robins, M. Saadatfar, O. Delgado-Friedrichs, and A. P. Sheppard, "Percolating length scales from topological persistence analysis of micro-CT images of porous materials," *Water Resour. Res.*, p. n/a-n/a, Dec. 2015.
[11] O. Delgado-Friedrichs, V. Robins, and A. Sheppard, "Skeletonization and Partitioning of Digital Images Using Discrete Morse Theory," *IEEE Trans. Pattern Anal. Mach. Intell.*, vol. 37, no. 3, pp. 654–666, Mar. 2015.
[12] H. Edelsbrunner, D. Letscher, and A. Zomorodian, "Topological Persistence and Simplification," *Discrete Comput. Geom.*, vol. 28, no. 4, pp. 511–533, 2002.
[13] M. Saadatfar, H. Takeuchi, V. Robins, N. Francois, and Y. Hiraoka, "Pore configuration landscape of granular crystallization," *Nat. Commun.*, vol. 8, p. 15082, May 2017.
[14] A. L. Herring, V. Robins, and A. P. Sheppard, "Topological Persistence of Pore Space and Nonwetting Phase in Sandstones," *Submitt. to Water Resour. Res.*, 2018.
[15] A. Sheppard, S. Latham, J. Middleton, A. Kingston, G. Myers, T. Varslot, A. Fogden, T. Sawkins, R. Cruikshank, M. Saadatfar, N. Francois, C. Arns, and T. Senden, "Techniques in helical scanning, dynamic imaging and image segmentation for improved quantitative analysis with X-ray micro-CT," *Nucl. Instruments Methods Phys. Res. Sect. B Beam Interact. with Mater. Atoms*, vol. 324, pp. 49–56, Apr. 2014.
[16] A. P. Sheppard, R. M. Sok, H. Averdunk, V. B. Robins, and A. Ghous, "Analysis of rock microstructure using high-resolution X-ray tomography," in *Proceedings of the International Symposium of the Society of Core Analysts*, 2006.
[17] N. R. Morrow, "Physics and Thermodynamics of Capillary Action in Porous Media," *Ind. Eng. Chem.*, vol. 62, no. 6, pp. 32–56, 1970.